Pergamon

Int. J. Heat Mass Transfer. Vol. 41, No. 13, pp. 2059–2071, 1998

Printed in Great Britain
0017-9310/98 $19.00+0.00

PII: S0017-9310(97)00286-X

Rotation effect on jet impingement heat transfer in smooth rectangular channels with heated target walls and radially outward cross flow

JAMES A. PARSONS and JE-CHIN HAN†

Turbine Heat Transfer Laboratory, Department of Mechanical Engineering, Texas A & M University, College Station, TX 77843-3123, U.S.A.

(*Received* 11 *April* 1996)

Abstract—The effect of rotation on jet impingement cooling by an inline array of circular jets in twin channels was studied. Impinging jets were in the direction of rotation in one channel and opposite to the rotation direction in the other channel. The jets impinged normally on the smooth, heated target wall in each channel. The flow exited the channels in a single direction, radially outward, creating cross flow on jets at larger radii. Jet rotation numbers and jet Reynolds numbers were varied from 0.0 to 0.0028 and 5000 to 10000, respectively. For the target walls with jet flow in the direction of rotation (or opposite to the direction of rotation), heat transfer decreased up to 15% (or 20%) as compared to corresponding results for non-rotating conditions. This is because the impinging jets were affected by the rotation-inducted secondary flows produced by Coriolis, buoyancy and centrifugal forces. © 1998 Elsevier Science Ltd. All rights reserved.

INTRODUCTION

In gas turbine engines as turbine inlet temperature increases engine thermal efficiency increases. However the amount of heat transferred to the turbine blades also increases. To achieve reasonable turbine blade durability goals the blades are cooled with air extracted from the compressor. Several cooling methods are employed such as: film cooling; augmented cooling in internal serpentine channels; and impingement cooling on internal blade surfaces. For advanced turbine design it is necessary to understand and to optimize for engine and turbine operating conditions, the cooling method employed, and the turbine blade geometry. A typical non-rotating turbine blade (stator) is hollow and may have a perforated insert pressurized with air that produces jets to impinge on and cool the interior surfaces of the blade. However, due to the design and the mechanical thermal stresses for rotating turbine blades, cooling these blades is more complicated. Rotation alters the motions of turbine blade internal coolant flow and hot external mainstream flow, and thus heat transfer in and around rotating turbine blades.

For the simple situation of a single circular jet impinging normally on a flat, non-rotating, solid wall (the target wall), the local Nusselt number ($Nu = hD/k$) depends on a large number of parameters. These parameters include: the jet Reynolds number ($Re_{jet} = \rho \bar{V}_j D/\mu$), the Prandtl number, the jet Mach number, the distance between the jet nozzle exit and the target wall, the angle of the jet axis to the target wall, and the local location on the target wall. In addition the nozzle type (i.e. orifice plate, a tube, or a contoured nozzle) [1], the jet turbulence level profile [2–4], the relative temperature difference across the shear layer between the jet fluid and the surrounding fluid [5–7], and the roughness of the target wall [8–11] affect the local surface heat transfer. References [12–16] present literature surveys on jet impingement heat transfer.

For the cooling design of non-rotating turbine vanes, important parameters such as the curvature of the target wall, the jet nozzle type, size and spacing for arrays of jets, and the exit flow configuration are important considerations [17–24]. The exit flow is constrained by the target wall, the jet wall (the wall containing the nozzles/holes that create the jets), and if used by additional wall(s) connecting these two walls. However, ref. [25] investigated impingement cooling by a single row of circular jets in the concave leading edge region of a rotating turbine blade with radially outward exiting cross flow. They presented heat transfer measurements for two model orientations: the jet direction was perpendicular to the direction of rotation and the jet direction was inclined at an angle of 60° to the direction of rotation. This and associated MIT GTL reports may be the only data available in open literature for rotating impingement heat transfer. They showed mean heat transfer decreased up to 30% relative to stationary results due to rotation

† Author to whom correspondence should be addressed.

NOMENCLATURE

A_w	exposed heated plate surface area
A_f	ratio of area of jets-to-exposed heated plate surface area (open area ratio)
D	impingement jet orifice diameter, 1.59 mm (0.0625 inch)
F	fluid body forces due to rotation
G	mass flux based on cross sectional area of flow
h	heat transfer coefficient
k	thermal conductivity of coolant (air)
Nu	local Nusselt number (hD/k) for rotating conditions
Nu_o	non-rotating local Nusselt number at corresponding location
q_{loss}	heat transfer rate from heated wall to test model
q_{total}	total heat transfer rate to heated wall
Re_{jet}	average jet hole Reynolds number ($\rho \bar{V}_j D/\mu$)
Ro	average jet rotation number ($\Omega D/\bar{V}_j$)
r_m	radial distance from axis of rotation to mean radius of test model
T_b	calculated bulk mean coolant temperature in channels
T_c	measured (and interpolated) coolant temperature in channels
T_j	inlet or jet temperature, $\approx$21–27°C
T_w	local wall (plate) temperature
V	local velocity
$\bar{V}$	average velocity
V_v	local vortical velocity
X	radially outward distance from test model inlet (see Fig. 2)
$(T_w - T_j)/T_w$	wall-to-coolant temperature difference normalized by absolute wall temperature [°R].

Greek symbols

μ	air dynamic viscosity
ρ	coolant density
Ω	rotational speed; rad s^{-1} in Ro and forces, rpm in figures.

Subscript

c	channel
COR	due to Coriolis force
CEN	due to centrifugal force
j	jet
w	wall (or plate).

induced buoyancy effects. Also local heat transfer distribution near the blade root changes significantly due to jet deflection caused by rotation for their operating ranges. They concluded rotation effects on heat transfer, if ignored, would cause large thermal stresses in turbine blades.

The goal of this investigation is to obtain heat transfer and flow distribution results for and thus extend the understanding of internal jet impingement cooling in channels under rotating conditions. Specifically, the objective is to determine the effect of rotation on pressure distributions (flow distributions) in and regional surface convective heat transfer on smooth target walls in rectangular cross sectioned, orthogonally rotating, twin channels with impingement cooling by square arrays of circular jets. Heat transfer measurements were obtained for the non-rotating test to compare the results with previous investigations.

TEST STAND AND MODEL

Figure 1 shows a test rig schematic. Regulated, compressed air (coolant), throttled by a flow control valve, flows through a sharp edge orifice flowmeter, through tubing, and through a rotating union at the bottom of a rotating shaft. The air then passes through the hollow rotating shaft and an aluminum, hollow rotating arm mounted perpendicularly onto the shaft. Finally the coolant passes through the test model and exits into the lab. The test model slips into one end of the arm and the other end serves as a counter balance. An electric motor with an adjustable frequency controller turns the shaft, arm, test model, a slip ring unit and a Scanivalve unit via a toothed belt. A digital photo tachometer measures the rotating shaft speed.

Figure 2 shows the channel walls of the test model are parallel or perpendicular to the axes of the rotating shaft and the arm, while a symmetry plane exits passing through these axes. The test model consists of twin channels of rectangular cross sections (2.18 cm × 0.64 cm) flanking (in and opposite to the direction of rotation) the square cross section supply channel (1.91 cm × 1.91 cm) at a mean rotating radius to jet diameter ratio of 397 and has a test model length to jet diameter ratio of 151.0. The jet diameter is 1.59 mm. Circular jet orifice holes of length to jet diameter ration of 5.2 are through the jet walls and connect the supply channel to each twin channel. The jet orifice holes create jets that impinge perpendicularly on the target walls with the distance between the jet hole exit and target wall to jet diameter ration of 4.0. The jet arrays for both twin channels are square with 30 rows in the radial direction with only two jets in each row for 60 jets per channel, 120 impinging jets in total. The distance between jet centers to jet diameter ratio is 5.0. In the test model, air first enters the supply chan-

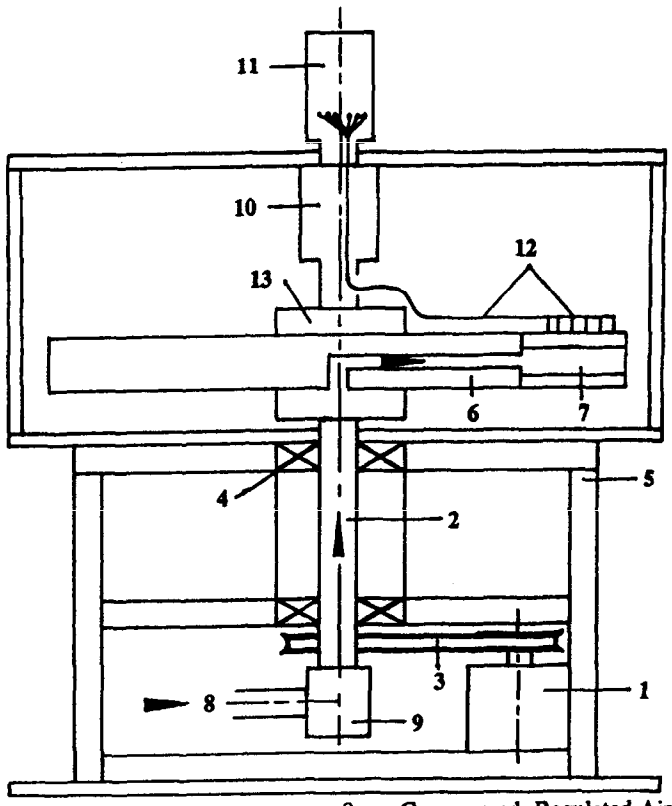

Fig. 1. Test stand schematic.

nel, flows through the 120 orifice holes, impinging on the target wall in the trailing channel and on the target wall in the leading channel. It finally exits the test model radially outward through one of two rectangular holes in the end cap of the arm.

Figure 2 shows the channel walls are each made of six isolated copper plate to obtain regionally averaged head transfer measurements. For each target wall plate, the face is 3.81 cm × 1.91 cm and the thickness is 3.2 mm. Ten jets are directly opposite each plate with jet area to target wall area ratio of 0.027. Each target wall is separately heated by wire resistance heaters uniformly cemented in grooves on the back side of the wall's copper plates. This creates a nearly uniform wall heat flux boundary condition during heat transfer experiments. The target wall copper plates are backed by Teflon of 2.5 cm. The other three walls in each of the twin channels are similar in construction, but remain unheated for tests in this paper. Thin 1.59 mm wide Teflon partitions separate and insulate the copper plates. Thermocouples (T-type, copper–constantan) with Teflon–Neflon PFA duplex insulation) in the plates measure wall temperatures while thermocouples in the center of all three channels measure local coolant temperatures. The thermocouples in the channels are at ends of wires protruding from on jet wall in the supply channel and from selected Teflon partitions of the jet walls in the heated channels (see Fig. 2). These wires remain perpendicular to the walls with coolant flow and rotation. An air passage of circular cross section (2.06 cm diameter) immediately upstream of the heated test model is made of Teflon for insulation. A slip ring unit mounts directly atop of a hub that connects the shaft to the arm. This 100 channel slip ring unit transfers thermocouple outputs to a data logger interfaced to a personal computer and variable transformer outputs to the wire resistance heaters.

Flow distribution measurements are obtained from six wall static pressure taps in each of the three channels. A nineteenth tap is at the inlet to the supply channel. Tubes from the taps are routed through the center of and connected to a Scanivalve unit mounted atop the slip ring unit. The Scanivalve unit contains a

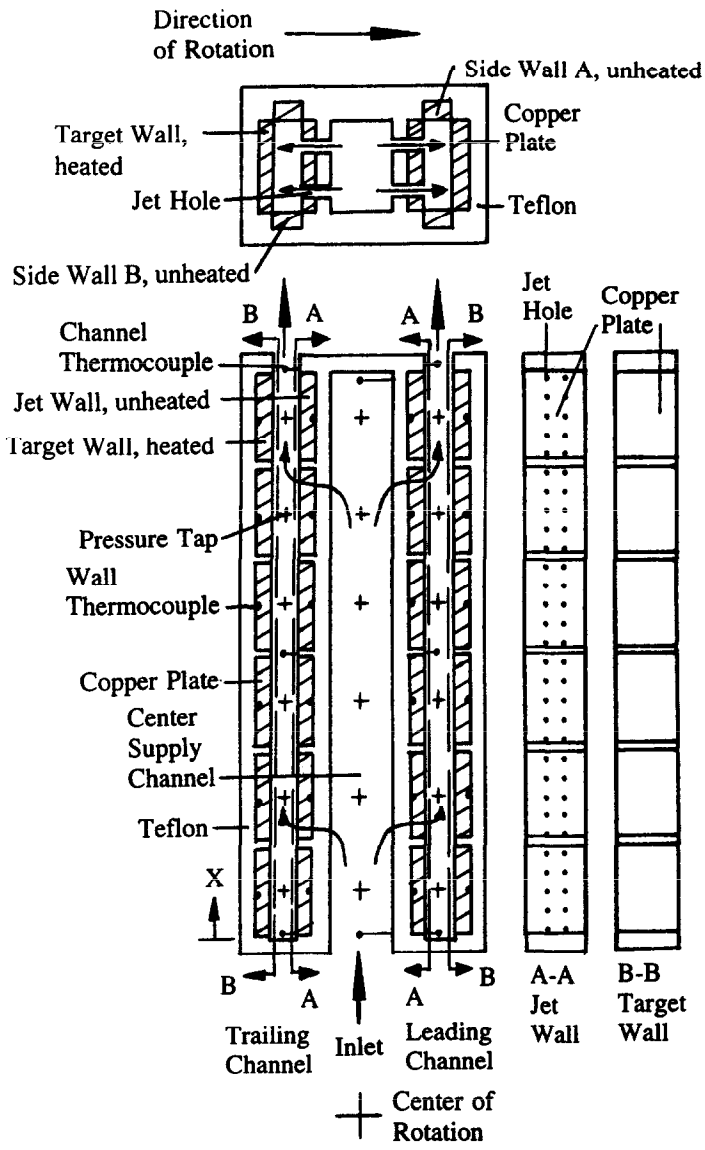

Fig. 2. Test model schematic.

multiport fluid switch, a stepper motor, a differential type pressure transducer, and an encoder. The multiport fluid switch connects only one pressure tap-port combination at a time to the transducer for pressure measurement. The motor moves the switch to different ports and the encoder indicates the selected tap-port. One additional port is connected to a u-tube manometer for transducer calibration. The Scanivalve motor control, input to and output from the pressure transducer, and output of the encoder are also via slip ring channels. The Scanivalve motor controller, the pressure transducer power supply and amplifier, a decoder that interprets the encoder output, the adjustable variac transformers that supply electric power to the heaters, the data logger, and voltage and amperage meters for measurements, are all located on a table next to the test stand.

TEST PROCEDURE AND DATA REDUCTION

The flow distribution tests are conducted adiabatically. This investigation assumes the mass flow distribution throughout the test model is relatively unchanged by heat addition during heat transfer tests. For flow tests, the rotating speed is set and then the throttle valve is adjusted for a desired total flowrate. An inclined manometer measures pressure drops across the sharp edge orifice flowmeter for total flow rate calculations. Finally, static pressure readings are recorded at all tap locations using the Scanivalve unit. Pre- and post-test pressure transducer calibrations are performed. For non-rotating flow tests, the leading and trailing channel exit pressures at the end cap holes are at atmospheric lab conditions. By interpolating for inlet and exit jet orifice hole pressures among the

measured channel pressures, the orifice pressure drops, the air jet velocities, the discharge coefficients and thus the flow rate ratio in each of the 120 orifice jets are calculated. Non-rotating and rotating discharge coefficients are calculated using the overall mass balance for the test model. The calculations assume one-dimensional flow and use ideal gas equation of state, continuity, and adiabatic compressible flow relations. For rotating tests, interpolations among channel pressures also determine the flow in each orifice. If a discrepancy occurs for overall mass balance the local discharge coefficients are adjusted in proportion to the amount of flow through each orifice. This preserves the slight increase of discharge coefficient with increasing Re_{jet}.

For heat transfer results, regional convective heat transfer coefficient h is:

$$h = (q_{total} - q_{loss})/[A_w(T_w - T_c)] \quad (1)$$

where q_{total} is the heat generated in a copper plate for heat transfer tests; q_{loss} is the heat loss for a plate; A_w is the heat target plate exposed surface area; T_w is a plate temperature; and T_c is a temperature for the coolant adjacent to the center of the heated plates which is obtained by spacial interpolation between measured local air temperatures. For heat transfer tests, the rotating speed and overall coolant flow rate are set and the transformers adjusted until the desired heated wall temperatures are reached. The plate and coolant temperatures, the voltages and currents for each heater, and the overall flowrate are recorded at steady state conditions. Then q_{total} (per plate) = voltage × current/6.0. The heat loss per plate (q_{loss}) is the amount of heat conducted into the test model and test stand but not convected directly to the coolant. Tests for heat loss are performed at the same rotating speed, with no coolant flow, and with the exit end cap holes covered with tape to prevent forced convection induced by rotation. Several input power levels are used to determine heat losses for all plates as functions of their corresponding temperature differences between each plate and the surroundings (room conditions).

The uncertainty of the local heat transfer depends on the net heat input ($q_{total} - q_{loss}$) to the coolant and the local wall-to-coolant temperature difference. This uncertainty increases with decreasing temperature difference and decreasing net heat input. Considering the method by ref. [26], the typical uncertainty in the Nusselt number is estimated less than ±8% for Re_{jet} = 10,000. However, the maximum uncertainty could be up to ±12% for Re_{jet} = 5000 at the largest radial location (X/D = 138). The heat conduction among a plate and its neighbors is estimated to be less than 1% of the net heat input for each plate at Re_{jet} = 5000. However, this percentage decreases to 0.5% at Re_{jet} = 10 000. For Re_{jet} = 5000, as the rotation rate increases from 0 to 800 rpm, the average ratios of the heat loss power to the total plate power increases from 0.09 to 0.16 for the target walls. At Re_{jet} = 10 000, these average ratios increase from 0.06 to 0.10 as rotation increases. The uncertainty in pressure difference decreases from 0.17% at Re_{jet} = 5000 to 0.11% at Re_{jet} = 10 000 of the maximum pressure difference for a jet Reynolds number.

EXPERIMENTAL RESULTS AND DISCUSSION

When considering test model geometry, the Nusselt number for target walls with jet impingement in rotating channels depends on: (1) the ratio of the test model's mean radius to jet diameter, (2) the ratio of local radial distance to jet diameter, (3) average jet Reynolds number, (4) Prandtl number, (5) jet rotation number, (6) wall-to-coolant temperature difference ratio, (7) jet flow direction with respect to rotation direction, and (8) channel geometry (cross section and orientation). The functional relationship is expressed as:

$$Nu = f(r_m/D, X/D, Re_{jet}, Pr, Ro, (T_w - T_j)/T_w, \text{jet direction, channel geometry}) \quad (2)$$

where Pr = 0.72 and r_m/D = 397. Operating conditions are: Re_{jet} = 5000 and 10 000, and Ω = 0, 400, and 800 rpm, combining to produce Ro = 0.0, 0.0008, 0.0015, and 0.0028. For the target walls, the wall-to-coolant temperature difference ratio is 0.0855 and 0.129 for 0 rpm, 0.129 for 400 rpm, and 0.0855 and 0.129 for 800 rpm. The other three walls in each of the twin channels are insulated and unheated. Air properties are at the film temperature (= $(T_c + T_w)/2$).

Flow distribution

Non-rotating results. For low speed flows in the non-rotating geometries, local velocity changes depend on pressure differences or gradients. Figure 3a shows channel static pressures versus channel location for the jet impinging flows under non-rotating conditions. However, Fig. 3b shows calculated mass fluxes G_c (= $\rho_c V_c$) for the channel cross flow direction and G_j (= $\rho_j V_j$) for the jet flow direction versus channel location. By observation, the trend of relative pressure differences among the three channel pressures for a Reynolds number are the same regardless of Reynolds number. Since leading and trailing channel pressures are the same for a Reynolds number, the supply-to-leading pressure differences and supply-to-trailing pressure differences are also the same. Thus, for each jet orifice location X/D the jet velocities and local jet mass fluxes G_j are the same from the supply channel toward the leading channel target wall and toward the trailing channel target wall. Orifice jet velocities and local jet mass fluxes increase with increasing channel position (X/D). For the supply channel, as the channel location increases the channel pressure increases slightly which indicates through flow velocity decreases (in the X direction). Mass flow calculations

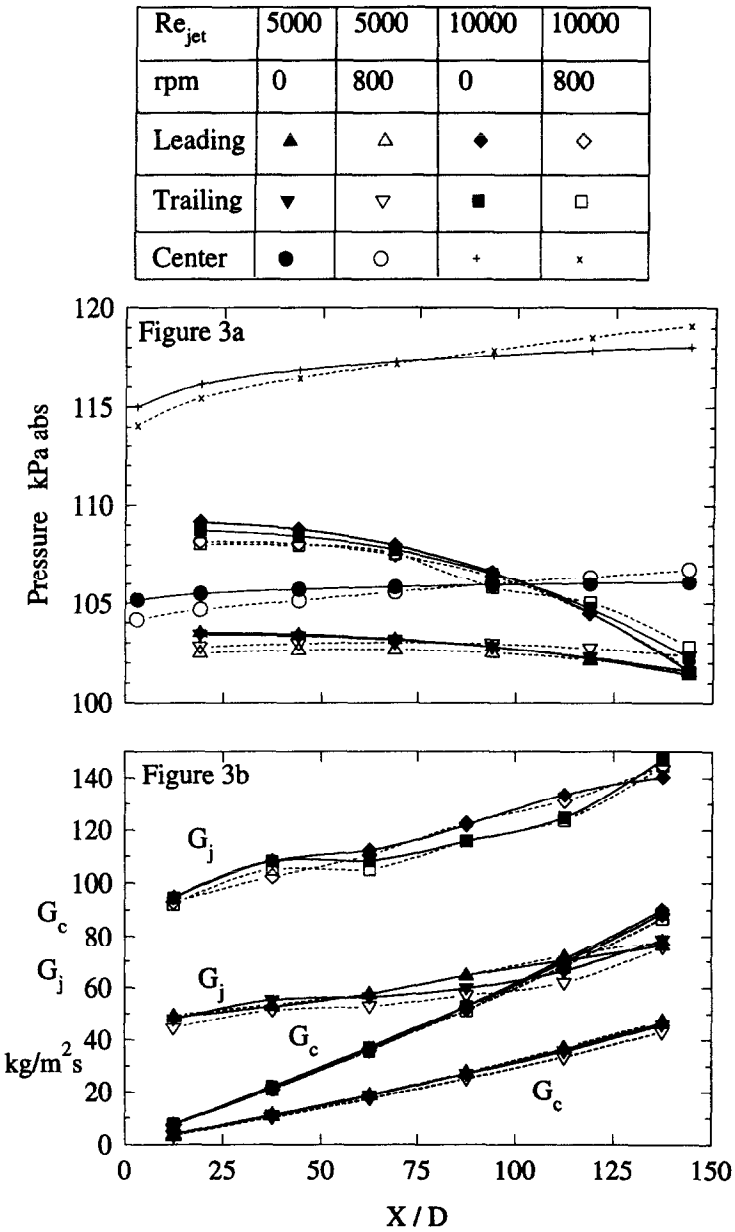

Fig. 3. Pressure and mass flux distributions for Re_{jet} = 5000 and 10 000 at Ω = 0 and 800 rpm.

for the supply channel verify this and the velocity is zero at the channel end (X/D = 151). The pressures decrease for the twin channel as channel location increases. Thus, cross flow velocities, the velocities in the X (or radial) direction in the twin channels, and the local channel mass fluxes G_c increase with channel location. The cross flow velocities and local channel mass fluxes are zero at X/D = 0.0. Thus, the flow distribution is symmetric for the non-rotating test model with respect to the supply channel centerline. Also, all velocities (supply through flow, jet and twin channel cross flow) and local mass fluxes (G_c and G_j) decrease as Re_{jet} decreases. Note the leading and trailing channel exit pressures are approximately equal for both Reynolds numbers under non-rotating conditions. From mass flow calculations the non-rotating discharge coefficients increase slightly as expected from 0.68 to 0.72 as local Re_{jet} increases from 3000 to 13 000, respectively. Also for Re_{jet} = 5000 and 10 000, the jet Reynolds numbers for all jets as well as the channel Reynolds numbers at almost all channel locations are in the turbulent regimes.

As an indicator for bending of jet flows, local blowing ratios (= G_j/G_c) and jet-to-cross flow momentum ratios (= $\rho_c G_j^2/(\rho_j G_c^2)$) are easily calculated from Fig. 3b since values for ρ_c/ρ_j are nearly 1.0. From film cooling studies as jet-to-cross flow momentum ratio decreases below 1.0, the jets bend in the channel flow

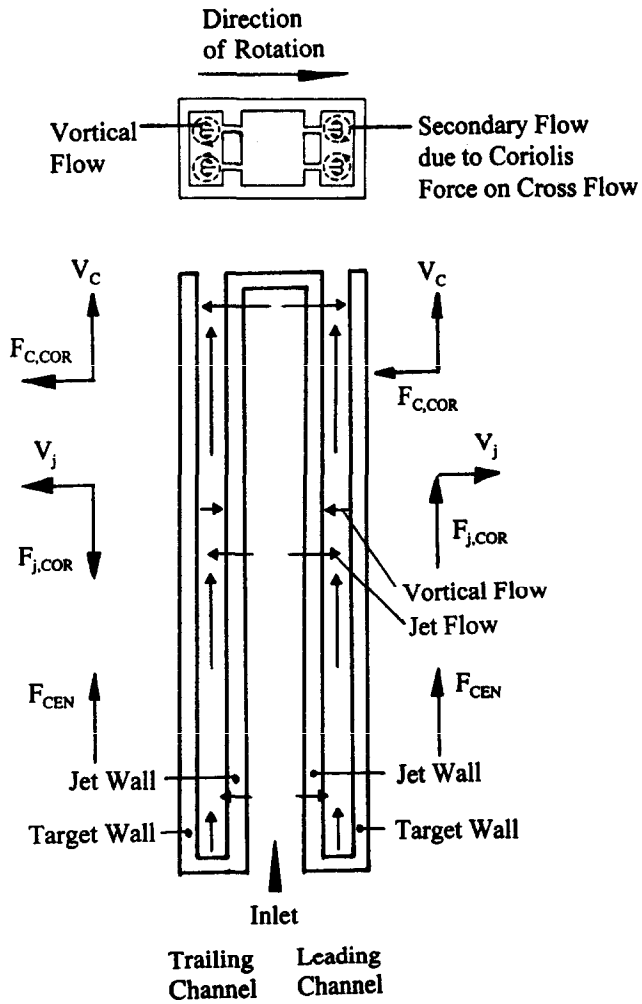

Fig. 4. Schematic including velocities and forces.

direction and attach to the jet wall. However in the present study, this momentum ratio remains above 2.5 even at $X/D = 138$ and $Re_{jet} = 10\,000$, the lowest value. Thus it is unlikely for jets to attach to the jet wall solely due to cross flow effects for both non-rotating and rotating conditions.

Rotating results. Flow distribution results for rotating tests are only slightly more complex than those for non-rotation. First as shown in Fig. 4, rotation produces centrifugal forces (radially outward), Coriolis forces (in various directions), and buoyancy forces (that depend on local air density/temperature variations) that create secondary flows and alter air flow in the test model. Second, as for solid body rotation, the pressure in the radial (i.e. X) direction increases with radius due to the pressure force opposing the fluid centrifugal force. Third, the channels act like radial vanes on a pump and transfer energy (in the form of pressure and/or velocity) to the air. Finally, the arm rotation creates complicated 3-dimensional flow and pressure fields around the end cap and thus by the leading and trailing channel exits. However it is believed that these channel exit flow conditions do not significantly affect the flow in the test model. Figure 4 also shows qualitative flow schematics for channel and jet flow velocities for non-rotating and rotating conditions.

Figures 3a and 3b also show pressure and local mass flux distributions, respectively, for rotating tests. Comparing the jet Reynolds numbers 5000 and 10 000, the pressure distributions are similar for rotations and non-rotation. The main difference is that the pressure difference from the inner radius ($X/D = 19$) to the outer radius ($X/D = 144$) for any channel and Reynolds number with rotation is approximately 1.5 kPa greater than their corresponding pressure differences without rotation. This is due to combined effects of the pressure force counteracting the fluid centrifugal force and of the pumping action of the channel. However, these additions are relatively small and the pressure differences and gradients for rotation remain nearly the same as those without. Also for these Reynolds numbers and rotation, the trailing channel exit pressure is about 850 Pa higher than the leading chan-

nel exit pressures. A close examination of Figs. 3a and 3b reveal that for rotating conditions nearly all of the velocities and mass fluxes for the leading channel are just slightly greater than those corresponding for the trailing channel. Thus orifice jet, supply channel through flow, and twin channel cross flow velocities, and local jet and channel mass fluxes for a jet Reynolds number are nearly the same with and without rotation. This indicates that rotation does not significantly alter the jet and channel flow distributions when compared with those results for non-rotation.

Heat transfer

Non-rotating results. Figure 5a shows the non-rotating target wall Nusselt number (Nu_o) versus channel location (X/D) for the Reynolds numbers at $(T_w - T_j)/T_w = 0.0855$. Additional test results for $(T_w - T_j)/T_w = 0.129$ (not plotted) are the same as their corresponding values for 0.0855. Thus the effect of buoyancy forces for non-rotating conditions are negligible. Second, for a jet Reynolds number the leading channel target wall Nu_o values are nearly the same as those for the trailing channel target wall. This confirms the test model operates symmetrically for flow and heat transfer under non-rotating conditions. Third, as Re_{jet} increases so do non-rotating Nusselt numbers. This is because heat transfer increases with an increase in jet and cross flow which reduces boundary layer thickness.

Figure 5a shows that as X/D increases, Nu_o initially decreases and then increases slightly at large X/D. This is explained as follows. Local convection heat transfer at the point of impingement is high and decreases as the distance from this point increases. This is due to decreasing target wall surface velocity gradients as jet fluid spreads on the target walls away from the point of impingement. However, as X/D increases, the magnitude of cross flow velocity V_c increases and bends jet flow away from the target walls towards the radially outward direction. This reduces locally high heat transfer at the point of impingement. Also, as the cross flow develops, the heat transfer initially decreases at

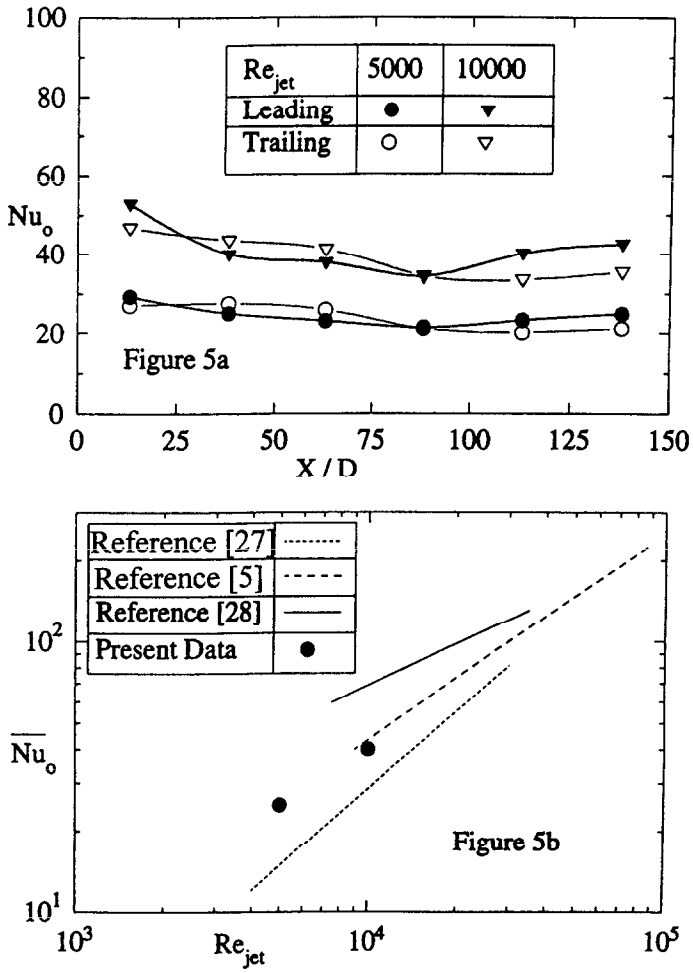

Fig. 5. Non-rotating results: (a) Nusselt number versus channel location for target wall at $(T_w - T_j)/T_w = 0.0855$; (b) wall average Nusselt number versus Re_{jet} for present data and comparison with other investigations.

small X/D as for developing flow at a channel entrance. Unlike channel flow, however, the heat transfer increases further downstream since the amount of cross flow increases as the result of added jet flow. This produces increasing velocity gradients at the surfaces that increase surface heat transfer. Also, it can be observed from Fig. 3 that the amount of jet flow (G_j) increases an X/D increases. Thus as X/D increases, regional heat transfer is initially high due to jet impingement, and decreases due to developing cross flow conditions and jet deflection. It then increases slightly at larger X/D due to the combined effects of jet deflection, added cross flow, and increased jet flow.

To show the integrity of the experimental method and test model, calculated bulk mean coolant temperature rises from overall energy balances are within 10 and 35% of the measured local air temperature rises for $Re_{jet} = 5000$ and 10000, respectively. Figure 5b shows Nu_o, the 12 plate average of Nu_o for the leading and trailing target walls, versus Re_{jet} under non-rotating conditions. Figure 5b also shows non-rotating target wall Nusselt numbers from two types of similar investigations. For the first type [5, 27] only the target wall is heated in the channel with the other walls unheated which is the same channel wall thermal boundary condition as the present data. The geometric parameters in [5] are ($D = 2.01$ mm, $A_f = 0.0201$, ratio of distance between jet plate and target wall-to-jet diameter = 1.0, and ratio of distance between jet centers-to-jet diameter = 6.25), whereas the geometric parameters in [27] are ($D = 3.18$ mm, $A_f = 0.0276$, ratio of distance between jet plate and target wall-to-jet diameter = 4.0, and ratio of distance between jet centers-to-jet diameter = 5.0). The Nusselt number values from the current investigation are comparable with the values obtained from [5]. However, the heat transfer values obtained from the current investigation are higher compared to the values from [27]. The second type [28] obtained detailed heat transfer measurements under minimum crossflow scheme, using a transient liquid crystal method with four isothermal channel walls. The geometric parameters in [28] are ($D = 5.08$ mm, ratio of distance between jet plane and target wall-to-jet diameter = 1.0, and ratio of distance between jet centers-to-jet diameter = 8.0). The heat transfer values obtained from [28] are higher compared to the values in the present study. The difference in results between various studies is due to different geometric parameters. In general for impingement heat transfer, Nu_o is proportional to Re_{jet}^m where $0.5 < m < 0.85$. The present data follows the same trend.

Rotating results. Effect of rotation relative to non-rotation. Figures 6a and 6b show the effect of rotation on the local Nusselt number ratio (Nu/Nu_o). Note that the Nusselt number ratio is the local Nusselt number divided by the corresponding measured local Nusselt number for non-rotation (see Fig. 5a). Figure 6a shows results for $Re_{jet} = 5000$ at rotation numbers $Ro = 0.0$, 0.0015 and 0.0028 ($\Omega = 0$, 400 and 800 rpm, respectively) and Fig. 6b shows results for $Re_{jet} = 10000$ at $Ro = 0.0$, 0.0008 and 0.0015 ($\Omega = 0.0$, 400 and 800, respectively). The results for $Re_{jet} = 5000$ ($Ro = 0.0015$ and 0.0028) show target wall Nusselt number ratios for the leading and trailing channels are below 1.0 (the non-rotating value) and between 0.80 and 0.95. At constant Re_{jet} as Ro increases ($Ro = 0.0015$ to 0.0028) the differences between these target wall Nusselt number ratios and 1.0 increase. In addition to the flow structures discussed above for non-rotating results, new secondary flows grow as rotation rate (Ω increases due to centrifugal forces ($\rho\Omega^2 r$), Coriolis forces ($\rho\Omega V_{local}$), and buoyancy forces ($\Delta\rho_{local}(\Omega^2 r + \Omega V_{local})$). For the leading channel, Fig. 4 shows the secondary flow due to the Coriolis force on the channel cross flow; two circular patterns in each channel. At the jet hole exit, this flow deflects jets away from the leading channel target wall. In addition the centrifugal force adds to the Coriolis force for jets towards the leading channel target wall to further bend jet flow away from the leading channel target wall. Also, the Coriolis force for the leading channel cross flow is directed away from and thus pulls air away from the leading channel target wall. But as channel location (X/D) increases, the cross flow velocity increases along with the Coriolis forces and the secondary flows. This increases the jet bending and the air pulling away from the leading channel target wall. Therefore these effects of rotation combine to thicken the boundary layer on the leading channel target wall and to decrease its heat transfer up to 15% as compared with those results for non-rotating conditions. For the trailing channel, the secondary flow due to the Coriolis force on the channel cross flow and the centrifugal force also bend jets away from the trailing channel target wall. However the Coriolis force for the trailing channel cross flow is towards the trailing channel target wall and tends to thin the boundary layer of this wall. And as for the leading channel, as channel location increases the velocities, forces and thus jet deflections increase. Therefore for the trailing channel target wall, the net effect of rotation is to decrease its Nusselt number ratio up to 20% as compared to corresponding non-rotating results.

Figure 6b for $Re_{jet} = 10000$ shows Nusselt number ratios for the target walls are below 1.0 but between 0.85 and 0.97. Also at constant $Re_{jet} = 10000$, as Ro increases the differences between the target wall Nusselt number ratios and 1.0 increase. However, these differences for lower rotation numbers (Fig. 6b) are reduced as compared to those differences as $Re_{jet} = 5000$ for higher rotation numbers (Fig. 6a). Therefore the effect of rotation (to reduce Nusselt number ratio) increases as Ro increases.

The results in Figs. 6a and 6b also show for larger channel locations ($X/D > 75$), the Nusselt number ratios for the leading channel target wall are generally larger than those Nusselt number ratios cor-

Re_{jet}		10000	10000	5000	5000
rpm	0	400	800	400	800
Ro	0	0.0008	0.0015	0.0015	0.0028
Leading	——	◆	▲	●	■
Trailing	——	◇	△	○	□

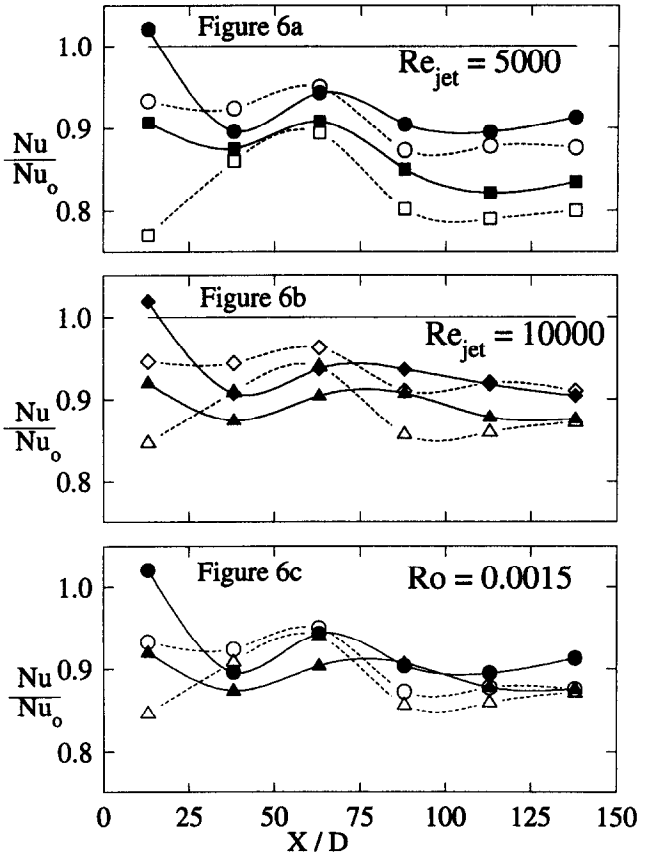

Fig. 6. Effect of rotation on target wall Nusselt number ratio at $(T_w - T_j)/T_w = 0.129$: (a) $Re_{jet}5000$; (b) $Re_{jet} = 10000$; (c) $Ro = 0.0015$.

responding for the trailing channel target wall. This is explained as follows. As channel location increases, the cross flow velocity increases (see Fig. 3b) and thus the Coriolis force for the channel cross flow also increases under rotating conditions. Figure 4 shows the secondary flows due to the Coriolis force on channel cross flow constructively combine with the jet vortical flow in the central region of the leading channel. However for the trailing channel these two flows combine destructively. Therefore for the leading channel, warm air is carried away from the target wall, thinning its boundary layer and enhancing its Nusselt number ratios as compared to those for the trailing channel target wall. There, the destructive combination of flows creates a relatively stagnant region of air next to the trailing channel target wall with relatively large boundary layers.

Effect of Reynolds number. Figure 6c shows the effect of Reynolds number on Nusselt number ratio while holding at $Ro = 0.0015$. The rotation number is held constant by varying the rotation speed Ω and $\bar{V}_j$ (or Re_{jet}): i.e. $\Omega = 400$ rpm, $Re_{jet} = 5000$ and $\Omega = 800$ rpm, $Re_{jet} = 10\,000$. The results show Nusselt number ratios are within 2% as either Reynolds number or rotation speed changes at constant rotation number for corresponding walls and channel locations. This supports the rotation number for use as a non-dimensional parameter for rotating impingement results.

Effect of wall-to-coolant temperature difference ratio. Figures 7a and 7b show the effect of the target wall-to-coolant temperature difference ratio $(T_w - T_j)/T_w$ on Nusselt number ratio for $Re_{jet} = 5000$, $Ro = 0.0028$ and for $Re_{jet} = 10\,000$, $Ro = 0.0015$, respectively. In Fig. 7a, the target wall Nusselt number ratios for the leading and trailing channels vary within 20% below 1.0. The main reason is the effect of

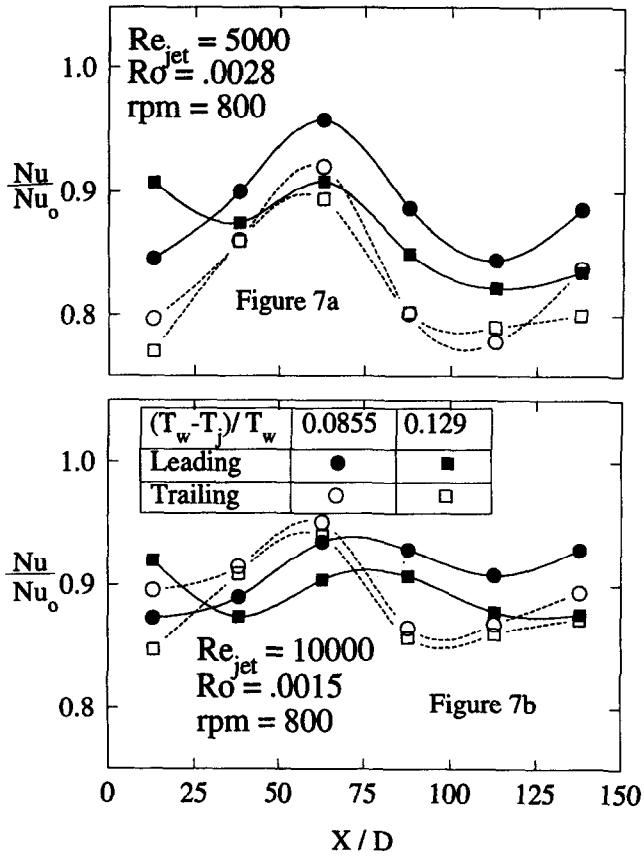

Fig. 7. Effect of wall-to-coolant temperature difference ratio on target wall Nusselt number ratio.

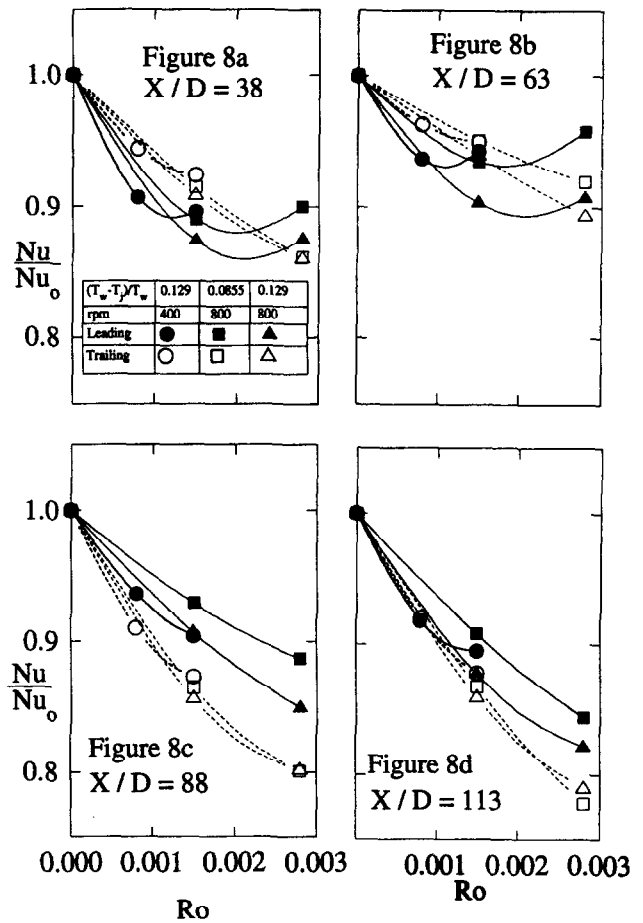

Fig. 8. Effect of rotation number and wall-to-coolant temperature difference ratio on target wall Nusselt number ratio: (a) $X/D = 38$; (b) $X/D = 63$; (c) $X/D = 88$; (d) $X/D = 113$.

rotation described above. However as $(T_w - T_j)/T_w$ increases the Nusselt number ratio generally decreases by up to 5% while other parameters are held constant. The jet, channel, and secondary flows and their corresponding Coriolis forces are in many directions and thoroughly mix the air in the channels. This produces small local variations of temperature and density. Recall the buoyancy body force $((\Delta\rho_{local}(\Omega^2 r + \Omega V_{local}))$ directly depends on local density variation. Thus as wall-to-coolant temperature difference ratio and thus local temperature and density variation increase, these buoyancy forces increase slightly and are in the same directions as those for local Coriolis and centrifugal forces. Therefore the effect of rotation discussed above (which is to reduce Nusselt number ratio as Ro increases) increases as $(T_w - T_j)/T_w$ increases.

Also in Fig. 7a, the differences between Nusselt number ratios for $(T_w - T_j)/T_w = 0.0855$ and 0.129 of the leading channel target wall are slightly larger than those corresponding differences of the trailing channel target wall. This is because for the leading channel, the constructive combination of flows in the channel's central region (mentioned above) enhances the buoyancy forces as compared to the destructive combination of flows (with reduced temperature and density variations) in the trailing channel.

In Fig. 7b results for $Re_{jet} = 10\,000$ and $Ro = 0.0015$ show the target wall Nusselt number ratios are at 1.0 or within 15% below 1.0, and as $(T_w - T_j)/T_w$ increases the Nusselt number ratios generally decrease up to 3% at $Ro = 0.0015$ (versus 5% at $Ro = 0.0028$ in Fig. 7a) while other parameters are held constant. Thus as discussed above the effect of rotation is reduced as Ro and as $(T_w - T_j)/T_w$ decrease.

Effects of rotation number and wall-to-coolant temperature difference ratio. Figures 8a, 8b, 8c and 8d show the effect of rotation number on Nusselt number ratio at channel locations $X/D = 38$, 63, 88 and 138, respectively. As discussed above the effect of rotation is to decrease Nusselt number ratios as rotation number increases. As discussed above the effect of rotation is to decrease Nusselt number ratios as rotation number $(Ro = \Omega D/V_j)$ is a key parameter to correlate rotation impingement Nusselt number ratios on both the leading and trailing target walls respectively. Figures 8a and 8b ($X/D = 38$ and 63) show as rotation number increases, the leading and trailing target wall Nusselt number ratios decrease by up to 14%. However, Figs. 8c and 8d ($X/D = 88$ and 113) show target wall Nusselt number ratios decrease by up to 17% for the leading channel and by up to 22% for the trailing channel, as rotation number increases. It is clear from these figures that for larger channel locations ($X/D > 75$), the constructive combination of flows mentioned above in the leading channel enhances Nusselt number ratios compared to those for the destructive combination of flows found in the trailing channels (lower Nusselt number ratios). Also, as the coolant-to-wall temperature difference ratio increases, the target wall Nusselt number ratio decreases for the leading channel and remains nearly constant for the trailing channel with other parameters held constant.

CONCLUSIONS

The main conclusions are as follows:

(1) For a square array of jets impinging normally on one wall in a rectangular channel with cross flow in one direction (radially outward) as the exit condition, jet and channel cross flow velocities increase as channel location increases. For a jet Reynolds number, pressure and thus flow distributions are almost the same with rotation as those without rotation.

(2) At constant jet Reynolds number and non-rotating conditions, as channel location increases, the leading and trailing target wall Nusselt numbers initially decrease and then slightly increase. For non-rotating conditions, the target wall averaged Nusselt numbers increase with jet Reynolds number and have the same trend as other researchers.

(3) As rotation number increases up to 0.0028, the target wall Nusselt number ratios for the leading (jet flow in the direction of rotation) and trailing (jet flow opposite to the direction of rotation) channels decrease up to 15 and 20%, respectively, below the non-rotating value of 1.0. This is because the impinging jets are affected by the rotation-induced secondary flows produced by Coriolis, buoyancy, and centrifugal forces.

(4) As wall-to-coolant temperature difference ratio $(T_w - T_j)/T_w$ increases from 0.0855 to 0.129 under rotating conditions, the target wall Nusselt number ratios decrease up to 5%.

(5) For parameter ranges in this paper, varying the jet Reynolds number while holding other parameters constant (Ro constant) had a small effect on target wall Nusselt number ratios for both channels.

Acknowledgements—This investigation was supported by the Texas Higher Education Coordinating Board—Advanced Technology Program under grant number 999903-165. This project was also supported by GE-Aircraft Engines. Their support is greatly appreciated.

REFERENCES

1. Gardon, R. and Cobonpue, J., Heat transfer between a flat plate and jets of air impinging on it. *International Developments in Heat Transfer, Proceedings of the 2nd International Heat Transfer Conference*, ASME, New York, NY, U.S.A., 1962, pp. 454–460.
2. Gardon, R. and Akfirat, J. C., The role of turbulence in determining the heat transfer characteristics of impinging jets. *Int. J. Heat Mass Transfer*, 1965, **8**, 1261–1272.
3. Wolf, D. H., Viskanta, R. and Incropera, F. P., Turbulence dissipation in a free-surface jet of water and its effect on local impingement heat transfer from a heated

surface: Part 1—Flow structure. *ASME J. Heat Transfer*, 1995, **117,** 85–94.
4. Wolf, D. H., Viskanta, R. and Incropera, F. P., Turbulence dissipation in a free-surface jet of water and its effect on local impingement heat transfer from a heated surface: Part 2—Local heat transfer. *ASME J. Heat Transfer*, 1995, **117,** 95–103.
5. Kercher, D. M. and Tabakoff, W., Heat transfer by a square array of round air jets impinging perpendicular to a flat surface including the effect of spent air. *ASME J. Engng Pwr*, 1970, **92,** 73–82.
6. Striegl, S. A. and Diller, T. E., Analysis of the effect of entrainment temperature on jet impingement heat transfer. *ASME J. Heat Transfer*, 1984, **106,** 804–810.
7. Bouchez, J. P. and Goldstein, R. J., Impingement cooling from a circular jet in a cross flow. *Int. J. Heat Mass Transfer*, 1975, **18,** 719–730.
8. Trabold, T. A. and Obot, N. T., Impingement heat transfer within arrays of circular jets, Part 2—Effects of cross flow in the presence of roughness elements. *ASME Paper No.* 87-*GT*-200, 1987.
9. Abdul Hussain, R. A. A. and Andrews, G. E., Enhanced full coverage impingement heat transfer with obstacles in the gap. *ASME Paper No.* 91-*GT*-346, 1991.
10. Gau, C. and Lee, C. C., Impingement cooling flow structure and heat transfer along rib-roughened walls. *Int. J. Heat Mass Transfer*, 1992, **35,** 3009–3020.
11. Priedeman, D., Callahan, V. and Webb, B. W., Enhancement of liquid jet impingement heat transfer with surface modifications. *ASME J. Heat Transfer*, 1994, **116,** 486–489.
12. Martin, H., Heat and mass transfer between impinging gas jets and solid surfaces, in *Advances in Heat Transfer*, **13,** ed. J. P. Harnett and T. F. Irvine Jr. Academic Press, New York, U.S.A., 1977, pp. 1–60.
13. Obot, N. T., Mujumdar, A. S. and Douglas, W. J. M., Design correlations for heat and mass transfer under various turbulent impinging jet configurations, *Drying '80*, **1.** Hemisphere, New York, U.S.A., 1980, pp. 388–402.
14. Hrycak, P., Heat transfer from impinging jets—a literature review. *AFWAL-TR*-81-3054, 1981.
15. Downs, S. J. and James, E. H., Jet impingement heat transfer—a literature survey. *ASME Paper No.* 87-*HT*-35, 1987.
16. Viskanta, R., Heat transfer to impinging isothermal gas and flame jets. *Experimental Thermal and Fluid Science*, 1993, **6,** 111–134.
17. Tabakoff, W. and Clevenger, W., Gas turbine blade heat transfer augmentation by impingement of air jets having various configurations. *ASME J. Engng Pwr*, 1972, **94,** 51–60.
18. Chupp, R. E., Helms, H. E., McFadden, P. W. and Brown, T. R., Evaluation of internal heat transfer coefficients for impingement cooled turbine blades. *AIAA J. Aircraft*, **6,** 203–208, *AIAA Paper No.* 68-564, 1969.
19. Metzger, D. E., Yamashita, T. and Jenkins, C. W., Impingement cooling of concave surfaces with lines of circular air jets. *ASME J. Engng Pwr*, 1969, **91,** 149–158.
20. Metzger, D. E., Baltzer, R. T. and Jenkins, C. W., Impingement cooling performance in gas turbine airfoils including effects of leading edge sharpness. *ASME J. Engng Pwr*, 1972, **94,** 219–225.
21. Hrycak, P., Heat transfer from a row of impinging jets to concave cylindrical surfaces. *Int. J. Heat Mass Transfer*, 1981, **24,** 407–419.
22. Metzger, D. E. and Bunker, R. S., Local heat transfer in internally cooled turbine airfoil leading edge regions: Part 2—Impingement cooling with film coolant extraction. *ASME J. Turbomachinery*, 1990, **112,** 459–466.
23. Bunker, R. S., and Metzger, D. E., Local heat transfer in internally cooled turbine airfoil leading edge regions: Part 1—Impingement cooling without film coolant extraction. *ASME J. Turbomachinery*, 1990, **112,** 451–458.
24. Gau, C. and Chung, C. M., Surface curvature effect on slot-air-jet impingement cooling flow and heat transfer process. *ASME J. Heat Transfer*, 1991, **113,** 858–864.
25. Epstein, A. H., Kerrebrock, J. L., Koo, J. J. and Preiser, U. Z., Rotational effects on impingement cooling, symposium on transport phenomena in rotation machinery. Honolulu, HI, U.S.A., 28 April–3 May 1985.
26. Kline, S. J. and McClintock, F. A., Describing uncertainties in single-sample experiments. *Mechanical Engineering*, 1953, **75,** 3–8.
27. Chance, J. L., Experimental investigation of air impingement heat transfer under an array of round jets. *TAPPI*, 1974, **57,** 108–112.
28. Van Treuren, K. W., Wang, Z., Ireland, P. T. and Jones, T. V., Detailed measurements of local heat transfer coefficient and adiabatic wall temperature beneath an array of impinging jets. *ASME Journal of Turbomachinery*, 1994, **116,** 369–374.